

Fast and Functional Structured Data Generators Rooted in Out-of-Equilibrium Physics

Alessandra Carbone

Sorbonne Université, CNRS, IBPS, Laboratoire de Biologie Computationnelle et Quantitative - UMR 7238, 75005 Paris, France.

Aurélien Decelle, Lorenzo Rosset,* and Beatriz Seoane

*Departamento de Física Teórica, Universidad Complutense de Madrid, 28040 Madrid, Spain. and
Université Paris-Saclay, CNRS, INRIA Tau team, LISN, 91190 Gif-sur-Yvette, France.*

(Dated: July 14, 2023)

In this study, we address the challenge of using energy-based models to produce high-quality, label-specific data in complex structured datasets, such as population genetics, RNA or protein sequences data. Traditional training methods encounter difficulties due to inefficient Markov chain Monte Carlo mixing, which affects the diversity of synthetic data and increases generation times. To address these issues, we use a novel training algorithm that exploits non-equilibrium effects. This approach, applied on the Restricted Boltzmann Machine, improves the model’s ability to correctly classify samples and generate high-quality synthetic data in only a few sampling steps. The effectiveness of this method is demonstrated by its successful application to four different types of data: handwritten digits, mutations of human genomes classified by continental origin, functionally characterized sequences of an enzyme protein family, and homologous RNA sequences from specific taxonomies.

I. INTRODUCTION

In recent years, many branches of science witnessed a rapid development and implementation of generative machine learning models, such as large language models for speech recognition and many more. In biology, significant progress has been made recently, for example, in designing artificial protein sequences with desired properties using deep learning networks [1–4]. The problem with these approaches is that they require a lot of data to train and are unable to generate sequences at the resolution level of subfamily-specific features due to the limited amount of data. Automatic classification of protein sequences according to their biological function based on a few examples is also a complex task because function cannot be inferred directly from phylogeny [5], and other sequence spaces have been defined for this end [6, 7]. In this work, we address the problem of classifying and generating sequences with a particular labeling prescription in a more general context using energy-based models (EBMs).

EBMs [8–11] are powerful generative models that encode a complex dataset distribution into the Boltzmann distribution of a given energy function. Their simplest versions, the Boltzmann [8] and the Restricted Boltzmann [9] machines, have recently got renewed attention in the scientific world, not only because they can generate high-quality synthetic samples in datasets for which convolutional layers offer no appreciable advantage [12–14], but also because they offer appealing modelling and interpretation capabilities while requiring relatively small training sets. Indeed, the trained model can be understood and studied as a physical interaction system to

model many-body distributions [15, 16], infer physical interactions [17, 18], extract patterns [19], or cluster [7]. The process of feature coding can also be analytically rationalized to some extent [20, 21]. EBMs, however, pose a major difficulty in training because the goodness of the trained models depends entirely on the quality of convergence to equilibrium of the Markov Chain Monte Carlo (MCMC) sampling used to estimate the log-likelihood gradient during training [22, 23]. These concerns are especially critical when dealing with highly structured datasets, as sampling multimodal distributions is particularly costly. This is because mixing times increase rapidly during training, which is dominated by barriers between metastable states. Non-ergodic MCMC sampling often leads to models that overrepresent certain modes at the equilibrium distribution level [22, 24]. This remains true if subsequent MCMC processes are initialized with the chain states used to compute the previous gradient update, the so-called persistent contrastive divergence (PCD) recipe [25]. Moreover, even perfectly trained models can be poor generators because they fail to reproduce all the diversity encoded in the probability measure because the chains cannot mix in a reasonable amount of time.

Recent works [22, 26, 27] have shown that if the task at interest is to generate new samples, it is easier to train EBMs using a non-convergent process, rather than to adjust the parameters of the Boltzmann distribution in such a way that equilibrium generated samples match the empirical distribution of the dataset. This means that EBMs can be trained to work as diffusion models [28], i.e., fast and accurate generators that perform a set of decoding tasks that can be impressed on the model during training. For structured datasets, this strategy offers two obvious advantages: the generated samples reflect better the diversity of the dataset, and the number of MCMC

* lrosset@ucm.es

steps needed to generate good-quality samples can be very short. Moreover, training out-of-equilibrium EBMs is not only faster than the standard procedure, but also stabler and easier to control [22]. Since this training strategy has been tested for the most part with image data, it has yet to be explored with highly structured datasets, where thermalization is prohibitively expensive.

In this paper, we show that Restricted Boltzmann Machines (RBMs) can be simultaneously trained to perform two different tasks after a few MCMC sweeps (just 10 in our experiments). First, they are able to generate samples conditioned on a particular label when initialized with random conditions. The samples generated by the model satisfy the individual label statistics with high accuracy and cover the entire data space in the correct proportion (Fig. 1-A). Second, they can accurately predict the label associated with a given sample (Fig.1-B). We validate our method on four different datasets: images of handwritten digits (MNIST), primarily to illustrate the method, and three highly structured datasets: one listing human DNA mutations in individuals and two others containing sequences of homologous protein and RNA families, respectively. For the latter sequence datasets, generating high-quality and feature-dependent data is usually challenging, if not impossible, in a reasonable amount of time.

The structure of this paper is as follows: we begin by introducing our EBM and the out-of-equilibrium training protocol. We then discuss our results in detail, coupled with an analysis of the tests performed to assess the quality of the generated samples. The paper concludes with a summary of our results and conclusions.

II. RESTRICTED BOLTZMANN MACHINE

Although RBMs have been around for a long time, they are largely used to describe aligned DNA, RNA or protein sequence datasets [13, 14, 19, 29, 30]. There are two reasons for this. First, convolutional layers are unlikely to provide much advantage in this case, and most importantly, they do not require many training examples to provide reliable results. The latter is especially important when dealing with semi-supervised tasks, since the number of manually curated entries is usually very small compared to the number and diversity of sequences available in public databases. We will devote all our work to this type of tasks and machines.

A. Definition of the model

The RBM is a Markov random field with pairwise interactions defined on a bipartite graph of two noninteracting layers of variables: the visible variables $\mathbf{v} = \{v_i\}_{i=1, \dots, N_v}$ represent the data, while the hidden variables $\mathbf{h} = \{h_\mu\}_{\mu=1, \dots, N_h}$ form a latent representation that models the effective interactions between the visi-

ble variables. The joint probability distribution of the visible and hidden variables is given by the Boltzmann distribution

$$p_{\boldsymbol{\theta}}(\mathbf{v}, \mathbf{h}) = \frac{1}{Z_{\boldsymbol{\theta}}} e^{-E_{\boldsymbol{\theta}}(\mathbf{v}, \mathbf{h})} \text{ with } Z_{\boldsymbol{\theta}} = \sum_{\mathbf{v}, \mathbf{h}} e^{-E_{\boldsymbol{\theta}}(\mathbf{v}, \mathbf{h})}. \quad (1)$$

In the previous expressions, the normalization factor $Z_{\boldsymbol{\theta}}$ is called the *partition function*, $\boldsymbol{\theta}$ refers to the parameters of the model and E is the energy function or *Hamiltonian*. In the simplest case, both the visible and the hidden units are binary variables, $v_i, h_\mu \in \{0, 1\}$, but we will also consider categorical (namely Potts) variables for v_i in the case of the homologous protein and RNA sequence datasets, see e.g. [7, 19] for a Potts version of the model. For the semi-supervised setting, we introduce an additional categorical variable in the visible layer, $\ell \in \{1, \dots, N_\ell\}$, that represents the label associated with the data point. That is, we follow the same scheme as in Ref. [31], but use a categorical variable for the label instead. We note that a very different procedure for conditional generation in RBMs have recently been proposed [32]. The associated Hamiltonian is

$$E_{\boldsymbol{\theta}}(\mathbf{v}, \mathbf{h}, \ell) = - \sum_i a_i v_i - \sum_\mu b_\mu h_\mu - \sum_{i\mu} v_i w_{i\mu} h_\mu - \sum_m c_m \delta_{\ell, m} - \sum_{m\mu} \delta_{\ell, m} d_{m\mu} h_\mu, \quad (2)$$

where $\delta_{\ell, m}$ is the Kronecker symbol that returns 1 if the label has the value m and 0 otherwise, $\mathbf{a} = \{a_i\}$, $\mathbf{b} = \{b_\mu\}$ and $\mathbf{c} = \{c_m\}$ are three sets of local fields acting respectively on the visible and hidden layers and on the label variable. $\mathbf{w} = \{w_{i\mu}\}$ is the *weight matrix* that models the interactions between visible and hidden layers, and $\mathbf{d} = \{d_{m\mu}\}$ is the *label matrix* that represents the interactions between the label and the hidden layer. The structure of the semi-supervised RBM is sketched in Fig. 2-A.

B. Out-of-equilibrium training

EBMs are generally trained by maximizing the Log-Likelihood (LL) function of the model computed on the dataset $\mathcal{D} = \{(\mathbf{v}^{(1)}, \ell^{(1)}), \dots, (\mathbf{v}^{(M)}, \ell^{(M)})\}$

$$\begin{aligned} \mathcal{L}(\boldsymbol{\theta}|\mathcal{D}) &= \frac{1}{M} \sum_{m=1}^M \log p_{\boldsymbol{\theta}}(\mathbf{v} = \mathbf{v}^{(m)}, \ell = \ell^{(m)}) \\ &= \frac{1}{M} \sum_{m=1}^M \log \sum_{\mathbf{h}} e^{-E_{\boldsymbol{\theta}}(\mathbf{v}^{(m)}, \mathbf{h}, \ell^{(m)})} - \log Z_{\boldsymbol{\theta}}, \end{aligned} \quad (3)$$

via (stochastic) gradient ascent. As usual, the gradient of \mathcal{L} is obtained by deriving it with respect to all parameters of the model (i.e., $\boldsymbol{\theta} = \{\mathbf{a}, \mathbf{b}, \mathbf{c}, \mathbf{d}, \mathbf{w}\}$ in our RBMs), which can be written as a subtraction of two terms:

$$\frac{\partial \mathcal{L}}{\partial \theta_i} = \left\langle -\frac{\partial E_{\boldsymbol{\theta}}}{\partial \theta_i} \right\rangle_{\mathcal{D}} - \left\langle -\frac{\partial E_{\boldsymbol{\theta}}}{\partial \theta_i} \right\rangle_E. \quad (4)$$

The symbols $\langle \cdot \rangle_{\mathcal{D}}$, and $\langle \cdot \rangle_E$ represent the average over the dataset and the model's Boltzmann measure described

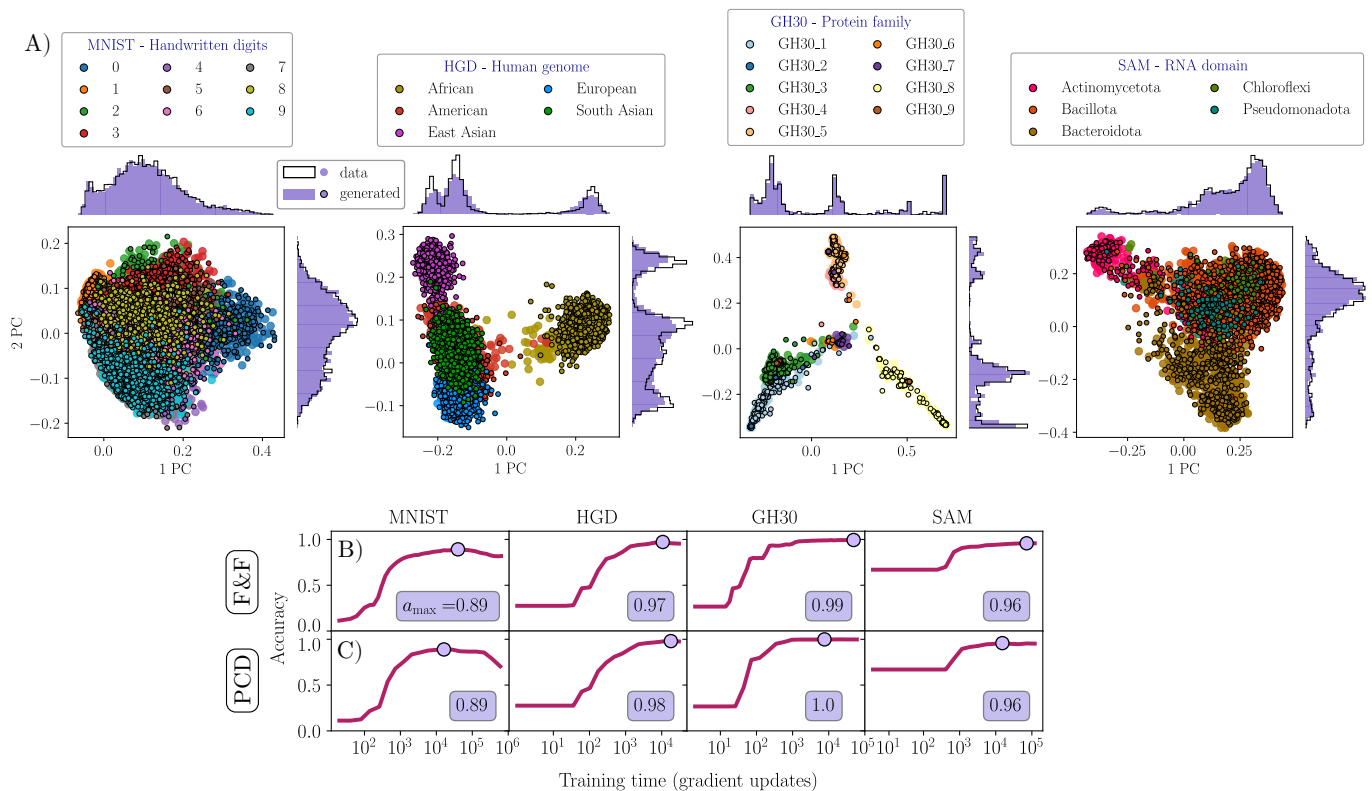


FIG. 1. A) Our F&F-10 model performs accurate conditional generation on a variety of datasets, as shown from left to right: (MNIST) handwritten digits classified by number, (HGD) mutations in the human genome classified by continental origin, (GH30) sequences from a homologous enzyme protein family characterized by different biological functions, and finally (SAM) a homologous family of RNA sequences classified by taxonomy. The generated samples are obtained by sampling the model equilibrium distribution for only 10 MCMC steps from a random initialization. The real and fake data are projected along the two principal components of the PCA of the dataset. Large dots indicate real data, while smaller contoured dots represent generated samples. Each color corresponds to a particular label. The synthetic dataset mirrors the structure of the real dataset, ensuring that each category has exactly the same number of entries. The histograms in the outer panels illustrate the distributions of the dataset (black outline) and the generated samples (violet-shaded area), projected along each of the main directions shown in the central scatter plot. Comparison of the accuracy's of B): F&F and C): PCD RBM in predicting the labels of samples in the test set as a function of the training time. The inference is done by starting from an initial random label and then performing 10^3 MCMC steps. The purple box in the corner of the insets indicates the maximum accuracy achieved (a_{\max}), corresponding to the big purple dot.

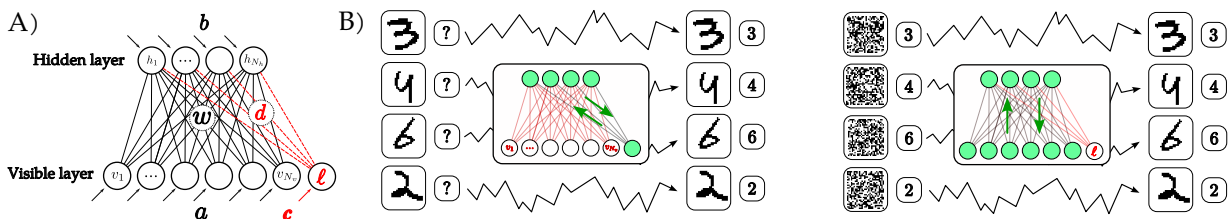


FIG. 2. A): Scheme of the semi-supervised RBM. B): Sketch of the sampling procedures used to calculate the two gradients during training. Left): label prediction. The visible layer is clamped to the data, while the labels are initialized randomly. The hidden layer and labels are sampled alternately using block-Gibbs sampling (green) and, after k MCMC steps, the model must provide the correct labels. Right): Conditional Sampling. The labels are fixed and the visible layer is initialized randomly. The model must generate a sample corresponding to the label in k MCMC steps.

in Eq. (1), respectively. One of the main challenges in training Energy-Based Models (EBMs) is computing a term on the right-hand side of Eq. (4), usually estimated via MCMC simulations. This term requires the Markov

chains to reach equilibrium—reflecting the Boltzmann measure—before statistical averages can be computed. This process can be very time-consuming, especially with complex datasets. The same issue comes up when gen-

erating new data samples according to the Boltzmann distribution. However, as mentioned in the introduction, there is a simple way around this problem [22, 26, 27].

The learning dynamics ruled by the gradient in Eq. (4) have a fixed point where the (generalized) *moments* of the distribution match those of the dataset, signified by $\langle -\partial E_{\theta}/\partial\theta_i \rangle_{\mathcal{D}} = \langle -\partial E_{\theta}/\partial\theta_i \rangle_E$. This indicates that even with accurate gradient computation during training—which is often not achievable—generation with these models is costly. It involves equilibrating the MCMC chains prior to generating good-quality samples. This becomes more challenging as the mixing times increase during training [22, 33]. An alternative approach suggests training the model to replicate the dataset’s moments not at equilibrium, but after a few sampling steps, say k , from an initial distribution \mathbf{p}_0 . This can be achieved by adjusting the gradient as

$$\frac{\partial \mathcal{L}^{\text{OOE}}}{\partial\theta_i} = \left\langle -\frac{\partial E_{\theta}}{\partial\theta_i} \right\rangle_{\mathcal{D}} - \left\langle -\frac{\partial E_{\theta}}{\partial\theta_i} \right\rangle_{p(k, \mathbf{p}_0)}. \quad (5)$$

Here, $p(k, \mathbf{p}_0)$ represents the non-stationary distribution of samples generated through an MCMC process that hasn’t reached equilibrium. The model trained this way is optimized to generate quality samples when sampled following the exact same procedure (at the fixed point): same update rules, initialization distribution and number of steps. This possibility has been recently proven rigorously [27], and experimentally validated in several studies across different EBMs [24, 26, 34], including RBMs [22].

In this paper, we will go one step further. We want to train the RBM to perform not one but two different generative tasks after only $k = 10$ MCMC sweeps by manipulating the chain initializations \mathbf{p}_0 . Specifically, we want to train the model to both synthesize (from random) samples of a given label, and to infer the correct label when given a dataset sample as chain initialization. To this end, we use two different out-of-equilibrium gradients in training, each designed for one of these tasks. The difference between the two correspond to the term $\langle \cdot \rangle_{p(k, \mathbf{p}_0)}$ in Eq. (5). For label prediction, this term is computed by clamping the visible layer onto the images/sequences in the training data and letting evolve the label configurations. For conditional generation, this term is computed using chains where the visible layer is randomly initialized and the labels are kept fixed to the labels in the training data. A sketch of the sampling procedures used to compute the two gradients can be found in the two panels of Fig. 2-B (label prediction, Fig. 2-B left; data generation, Fig. 2-B right). We refer to the models trained in this way as F&F-10 RBMs, where the 10 represents the number of MCMC steps k used to estimate the gradient at each parameter update. The model and hyperparameters used for the training are listed in Tab. II of Appendix C.

For comparison, we will also train our RBMs using the standard PCD recipe [25] with a large number $k = 100$ of sampling steps by gradient update to try to promote thermalization of the Markov chains as much as possible

during training. We will refer to this training procedure as PCD-100. In this training scheme, both the variables and the labels evolve together during sampling, and the last configurations reached after each parameter update are used as initialization for the chains of the subsequent one, which is commonly referred as the permanent or persistent chain. Furthermore, we train the F&F-10 and PCD-100 RBMs under the same conditions: same training sets, training epochs, learning rate, and mini-batch size. Since the PCD-100 requires 10 times more sampling steps per update, it is important to emphasize that PCD training takes 10 times longer than the F&F.

III. RESULTS

We applied the F&F RBM to four labeled data sets. First, MNIST [35], which contains images of handwritten digits along with their respective number, so that we can easily introduce the method and visually assess the quality of the conditional generation. Second, the Human Genome Dataset (HGD) [36], comprising binary vectors representing a human individual with 1s or 0s indicating gene mutation relative to a reference sequence. Labels here signify the individual’s continental origin. Third, the GH30 enzyme protein family dataset, as a benchmark for the model’s capability to generate artificial protein sequences having a subfamily-specific biological function trained using natural sequences classified in the CAZy database [37]. Finally, the S-adenosylmethionine (SAM) dataset, which consists of homologous RNA sequences of the aptamer domain of the SAMI riboswitch, for which taxonomic classification is known. These three datasets allow us to test our method on real biological data of interest with different levels (and nature) of characterization. Detailed explanations of these datasets are available in Appendix A.

Classification task – Figs. 1-B and C illustrate the label prediction accuracy for the test set over training time using both F&F and PCD training protocols. In our experiments we find that, with both training schemes, the models are able to reach very good accuracies for all the considered datasets, never below 0.89 and compatible between training schemes. Interestingly, we find that the best performance of the F&F RBM is not achieved at the same number of MCMC steps used for the training, but grows very rapidly and then stabilizes without displaying any out-of-equilibrium effects. We show the prediction accuracy over sampling time t_G for both training protocols in Fig. 9 of Appendix E. We would like to emphasize that our PCD-RBMs perform well for the label prediction task even in cases where they are not able to conditionally generate new samples, as we will show later, consistently with the good classification results obtained in Ref. [31]. The confusion matrices from label prediction for all datasets are gathered in Appendix E, Fig. 7.

Conditioned Generation task – We show in Fig. 1-A a projection of the samples generated after just 10 MCMC

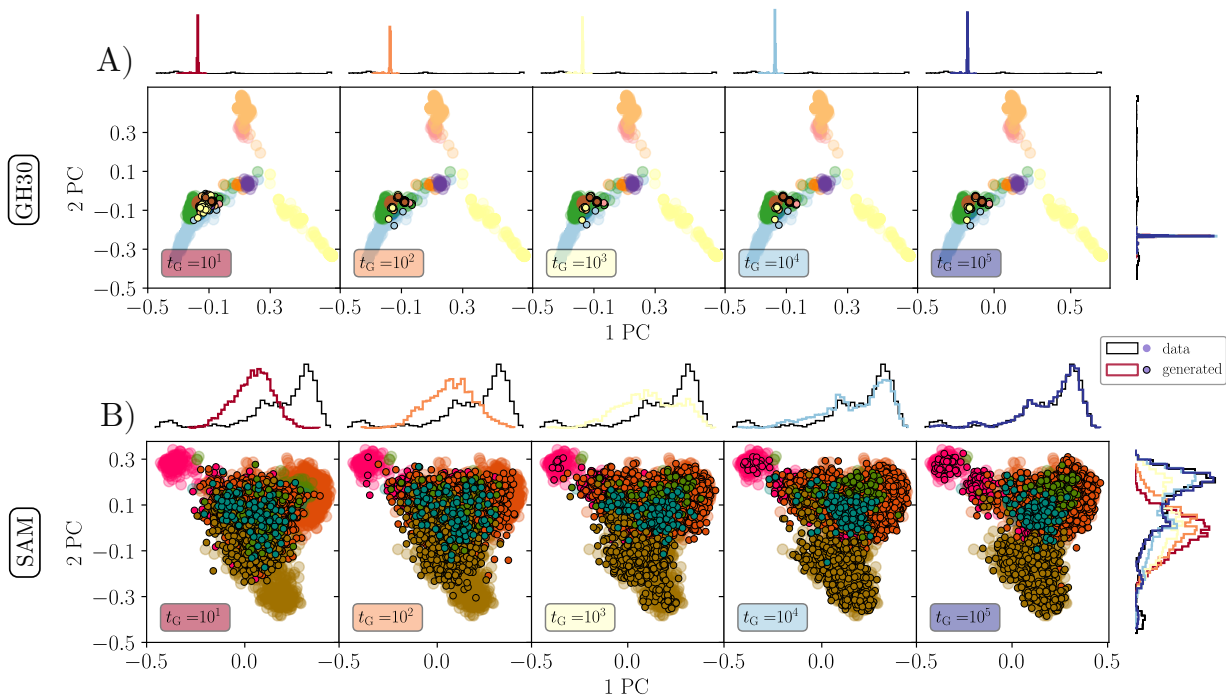


FIG. 3. Difficulties in generation with RBMs trained with the PCD-100 protocol. In both panels, we show from left to right the projection on the first two main directions of the dataset of generated samples conditioned on a given label after a different number of sampling steps $t_G = 10, 100, 1000, 10^4$ and 10^5 respectively. As in Fig. 1, each point represents a sample, the labels are shown in different colors, and the synthetic data are highlighted by an outer black ring. In the lateral margins, we show the histograms of the projections along each of the two directions: in black the dataset and the colors refer to the samples generated at different sampling times t_G . In A) we show the results for a dataset where PCD training was unstable, the GH30 dataset. Even up to $t_G = 10^5$, the sampling suffers from strong mode collapse. In B) we show data obtained when training the SAM dataset, where the PCD-100 training leads to a good generative model. We see that in this case, good quality samples that reproduce the statistics of the dataset are generated only after 10^5 MCMC steps.

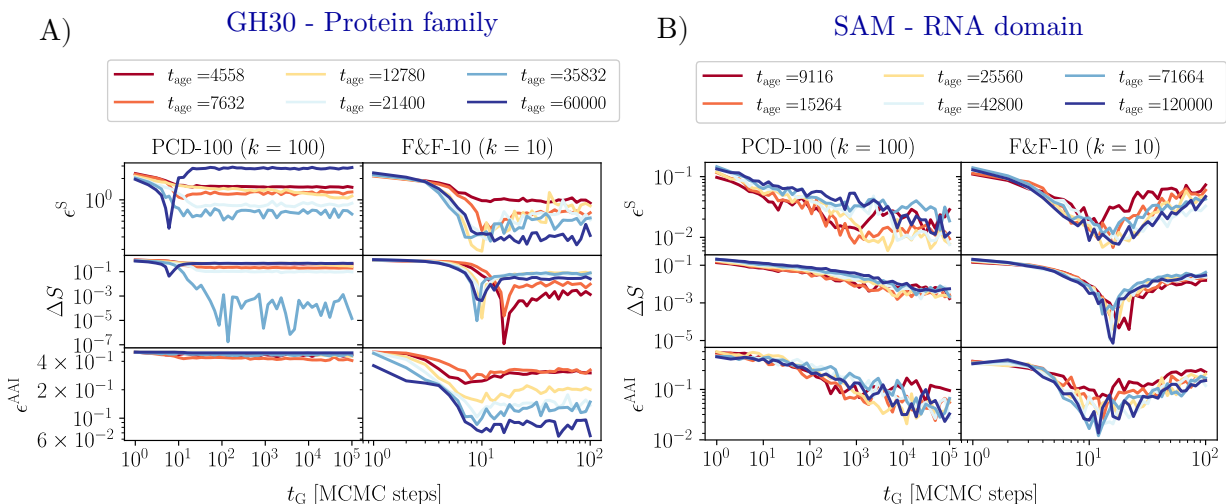


FIG. 4. Comparison of the scores on the generated data between PCD-100 and F&F-10 RBMs as a function of the generation time (t_G) for A) GH30 and B) SAM. All the scores are computed by comparing the test set with an identical (in terms of samples for each category) generated dataset. The samples of each category of the dataset have been compared with the corresponding samples of the synthetic data, and the curves shown in the figure represent the average scores across the different categories. The different colours of the curves represent different training times (t_{age}), expressed in terms of gradient updates. Notice that for the PCD-RBM the generation time ranges up to 10^5 MCMC updates, while for the F&F-RBM it only reaches 10^2 MCMC updates. The generated samples shown in Figs. 1 and 3 correspond to the darkest blue curves in correspondence of the indicated generation time t_G .

steps with a given label onto the first two principal di- rections of each dataset using the F&F. The F&F model

effectively generates data within a few MCMC steps that satisfy the target labels and cover the entire data space following a very similar distribution to the original data, as can be seen from the comparison of the histograms in the figure. In the case of the PCD-100 RBM, the situation is somewhat different. First, we find that the trainings are quite unstable depending on the hyperparameters used. For example, by changing the number of hidden nodes we get RBMs that are either good or completely unusable generative models when adopting the same training scheme, as we discuss in Fig. 11 of Appendix E for the SAM dataset. Moreover, we were not able at all to properly obtain generative PCD-100 RBMs for the MNIST and GH30 datasets, as we illustrate in Fig. 3–A. The figure shows the projection of the samples generated by the PCD-100 RBM for the protein sequence dataset, for which the Markov chains remain trapped in a very small region of the data space and the machine never generates reliable sequences within 10^5 MCMC steps. Conversely, the time required to generate sufficiently diverse samples when a working PCD RBM is found, as in the RNA dataset, is extremely long, see Fig. 3–B, where the *Actinomyces* sequences (pink cluster top left) are generated only after 10^5 MCMC steps. This is to be compared with the 10 MCMC required with the F&F-10 RBM shown in Fig. 1–A (which also requires 10 times less time to train).

To further assess the generated data’s quality, we used several error scores comparing synthetic and real data properties over the sampling time. These scores examine error in the covariance matrix spectrum, ϵ^S , diversity via an entropy measure, ΔS , and mode collapse and overfitting using the Adversarial Accuracy Indicator [38], ϵ^{AAI} . In all four cases, the score is always positive and the perfect generation corresponds to an error of zero. Detailed definitions are found in Appendix D. In Fig. 4, we show the evolution of these scores (for datasets GH30 and SAM) obtained when sampling configurations starting from random conditions using PCD-100 and F&F-10 RBMs, plotted as a function of the MCMC generation sampling time (t_G). The results for the MNIST and HGD datasets are shown in Fig. 10 in Appendix E. As expected, the F&F-10 RBMs develop a best-quality peak around $t_G \sim 10$, the k used for training, while the PCD-100 runs show a very slow relaxation behaviour eventually reaching good quality values at long sampling times in the case of the HGD and SAM datasets, as discussed in Fig. 3–B, or show a clear problem in generative performance with very poor scores (MNIST and GH30 datasets) and bad generated samples, as shown in the projections of Fig. 3–A and visually in Fig. 8 of Appendix E for MNIST.

Interestingly, based on previous experience with these datasets without label monitoring, we found the poor performance of the semi-supervised PCD-100 on MNIST training very surprising, since PCD usually performs quite well on this dataset (see, for example, [22]). The only explanation we have is that the addition of labels seems to greatly increase the mixing times, as can be seen in Fig. 10–A of Appendix E. A similar situation is found

with the SAM dataset when 1000 hidden nodes are used, see Fig. 11–B of Appendix E, but not with 100 hidden nodes. It is possible that a working setting can also be found for the MNIST dataset, but we did not succeed in our trials. In any case, this difficulty may explain why previous similar approaches that addressed classification using RBMs [31] focused only on the classification task and did not consider the conditional generation performance. Conversely, even though the HGD is typically a challenging benchmark dataset for classical equilibrium RBM models [39], our semi-supervised training yielded very high-quality models with thermalization times of only a few hundred MCMC steps. Altogether, these results show that classical training of RBMs with PCD for conditional generation is unreliable because it is difficult to control the risks of very poor generation performance. In contrast, the F&F model proved to be robust and reliable for all tested highly structured datasets. It produced high-quality artificial data after only a few MCMC steps, while requiring a significantly shorter training time.

We can also examine the quality of the samples generated by the F&F-10 RBM, but this time for each label, see Fig. 5. Again, the highest quality samples of each category are generated in about 10 steps, the same number of steps used for gradient estimation during training. It is interesting to point out that the F&F-10 RBM generates good quality samples even for categories in which it has seen only a few examples ($\lesssim 100$) in the training set. The number of samples in the training/test sets for each dataset and category can be found in Table I of Appendix C.

For an indirect and more biologically relevant measure of generated protein sequences’ quality, we extensively assessed their predicted three-dimensional structure using the ESMFold [40], comparing these predictions with those obtained with the test set. Specifically, we created histograms for both the generated sequences and the test set based on the frequency of predicted pLDDT scores from ESMFold, indicating the average confidence in the folding. Given a reference protein structure and a structure predicted by a model, the LDDT (Local Distance Difference Test) score assesses how well local atomic interactions in the reference protein structure are reproduced in the prediction. The pLDDT (predicted LDDT) score is returned by the ESMFold model, and it allows us to evaluate the degree of confidence of a folding even without having the reference structure. These distributions are displayed in Fig. 6 showing a remarkable agreement supporting the idea that we are generating structurally reliable and biologically relevant protein sequences but experimental tests are needed to confirm the biological classification.

IV. CONCLUSIONS

In this study, we used a unique method for training RBMs to embed the statistics of the datasets into

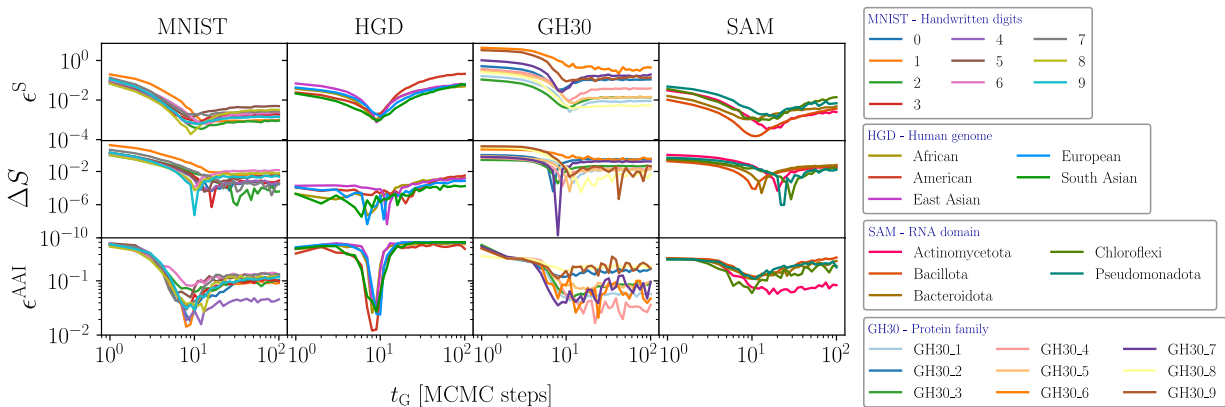


FIG. 5. For each of the datasets considered, we show the evolution of three different quality scores as a function of sampling generation time, t_G , for each label separately. The first row shows the error on the eigenvalue spectra, the second row shows the error on the entropy, and the third row shows the Adversarial Accuracy Indicator. For the GH30 and the SAM datasets, we used the training set to generate the error curves because there was too limited data in the test set to compare certain categories. The definition of the scores can be found in Appendix D.

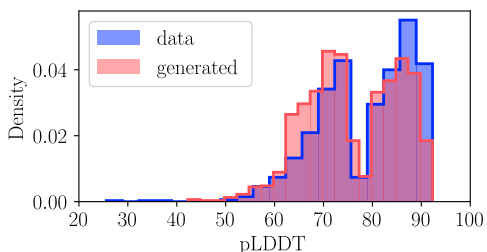


FIG. 6. Histograms of the confidence on the predicted folding structure of GH30 (based on the pLDDT score) for generated data (red) and real data (blue). The generated set consists of 150 samples per each of the 9 categories.

the nonstationary distributions of a Markov chain process [22, 26, 27], in contrast to conventional methods that encode information only at the equilibrium measure level. This strategy allows us to use RBMs as efficient generators, similar to diffusion models, with the added benefit

that various generative tasks can be easily encoded into the model. In particular, we trained RBMs to generate label-conditioned samples in a minimal number of sampling steps— a process that is typically tedious and slow in conventional methods— and derive the good label when Markov chains are randomly initialized. We have shown that our approach successfully generates high-quality synthetic samples that accurately reflect the full diversity of the dataset even for highly structured data, overcoming the limitations of standard (equilibrium) training methods while requiring shorter training times and displaying better stability. Noticeably, our method proved to be able to generate artificial protein sequences covering the full data space across subfamilies with different functionality, a particularly challenging task. Last but not least, the two-gradient method presented here can be easily implemented in EBMs having a more elaborated energy function (convolutional layers, ...) to model other complex datasets.

-
- [1] E. C. Alley, G. Khimulya, S. Biswas, M. AlQuraishi, and G. M. Church, Unified rational protein engineering with sequence-based deep representation learning, *Nature methods* **16**, 1315 (2019).
 - [2] J.-E. Shin, A. J. Riesselman, A. W. Kollasch, C. McMahon, E. Simon, C. Sander, A. Manglik, A. C. Kruse, and D. S. Marks, Protein design and variant prediction using autoregressive generative models, *Nature communications* **12**, 2403 (2021).
 - [3] I. Anishchenko, S. J. Pellock, T. M. Chidyausiku, T. A. Ramelot, S. Ovchinnikov, J. Hao, K. Bafna, C. Norn, A. Kang, A. K. Bera, *et al.*, De novo protein design by deep network hallucination, *Nature* **600**, 547 (2021).
 - [4] L. Moffat, S. M. Kandathil, and D. T. Jones, Design in the dark: learning deep generative models for de novo protein design, *bioRxiv*, 2022 (2022).
 - [5] F. Pazos, A. Rausell, and A. Valencia, Phylogeny-independent detection of functional residues, *Bioinformatics* **22**, 1440 (2006).
 - [6] R. Vicedomini, J. Bouly, E. Laine, A. Falcioratore, and A. Carbone, Multiple profile models extract features from protein sequence data and resolve functional diversity of very different protein families, *Molecular biology and evolution* **39**, msac070 (2022).
 - [7] A. Decelle, L. Rosset, and B. Seoane, Unsupervised hierarchical clustering using the learning dynamics of rbms, *arXiv preprint arXiv:2302.01851* (2023).
 - [8] D. H. Ackley, G. E. Hinton, and T. J. Sejnowski, A learning algorithm for boltzmann machines, *Cognitive science* **9**, 147 (1985).

- [9] P. Smolensky, *Parallel Distributed Processing: Explorations in the Microstructure of Cognition: Foundations*, Vol. 6 (1987) pp. 194–281.
- [10] Y. LeCun, S. Chopra, R. Hadsell, M. Ranzato, and F. Huang, A tutorial on energy-based learning, Predicting structured data **1** (2006).
- [11] J. Xie, Y. Lu, S.-C. Zhu, and Y. Wu, A theory of generative convnet, in *International Conference on Machine Learning* (PMLR, 2016) pp. 2635–2644.
- [12] S. Cocco, C. Feinauer, M. Figliuzzi, R. Monasson, and M. Weigt, Inverse statistical physics of protein sequences: a key issues review, Reports on Progress in Physics **81**, 032601 (2018).
- [13] B. Yelmen, A. Decelle, L. Ongaro, D. Marnetto, C. Tallec, F. Montinaro, C. Furtlehner, L. Pagani, and F. Jay, Creating artificial human genomes using generative neural networks, PLoS genetics **17**, e1009303 (2021).
- [14] B. Yelmen, A. Decelle, L. L. Boulos, A. Szatkownik, C. Furtlehner, G. Charpiat, and F. Jay, Deep convolutional and conditional neural networks for large-scale genomic data generation, bioRxiv , 2023 (2023).
- [15] G. Carleo and M. Troyer, Solving the quantum many-body problem with artificial neural networks, Science **355**, 602 (2017).
- [16] R. G. Melko, G. Carleo, J. Carrasquilla, and J. I. Cirac, Restricted boltzmann machines in quantum physics, Nature Physics **15**, 887 (2019).
- [17] M. Weigt, R. A. White, H. Szurmant, J. A. Hoch, and T. Hwa, Identification of direct residue contacts in protein-protein interaction by message passing, Proceedings of the National Academy of Sciences **106**, 67 (2009).
- [18] F. Morcos, A. Pagnani, B. Lunt, A. Bertolino, D. S. Marks, C. Sander, R. Zecchina, J. N. Onuchic, T. Hwa, and M. Weigt, Direct-coupling analysis of residue coevolution captures native contacts across many protein families, Proceedings of the National Academy of Sciences **108**, E1293 (2011).
- [19] J. Tubiana, S. Cocco, and R. Monasson, Learning protein constitutive motifs from sequence data, Elife **8**, e39397 (2019).
- [20] A. Decelle and C. Furtlehner, Restricted boltzmann machine: Recent advances and mean-field theory, Chinese Physics B **30**, 040202 (2021).
- [21] A. Decelle, G. Fissore, and C. Furtlehner, Spectral dynamics of learning in restricted boltzmann machines, EPL (Europhysics Letters) **119**, 60001 (2017).
- [22] A. Decelle, C. Furtlehner, and B. Seoane, Equilibrium and non-equilibrium regimes in the learning of restricted boltzmann machines, Advances in Neural Information Processing Systems **34**, 5345 (2021).
- [23] E. Nijkamp, R. Gao, P. Sountsov, S. Vasudevan, B. Pang, S.-C. Zhu, and Y. N. Wu, Mcmc should mix: learning energy-based model with neural transport latent space mcmc., in *International Conference on Learning Representations (ICLR 2022)*. (2022).
- [24] E. Nijkamp, M. Hill, T. Han, S.-C. Zhu, and Y. N. Wu, On the anatomy of mcmc-based maximum likelihood learning of energy-based models, Proceedings of the AAAI Conference on Artificial Intelligence **34**, 5272 (2020).
- [25] T. Tieleman, Training restricted Boltzmann machines using approximations to the likelihood gradient, in *Proceedings of the 25th international conference on Machine learning* (2008) pp. 1064–1071.
- [26] E. Nijkamp, M. Hill, S.-C. Zhu, and Y. N. Wu, Learning non-convergent non-persistent short-run mcmc toward energy-based model, in *Advances in Neural Information Processing Systems*, Vol. 32, edited by H. Wallach, H. Larochelle, A. Beygelzimer, F. d'Alché-Buc, E. Fox, and R. Garnett (Curran Associates, Inc., 2019).
- [27] E. Agoritsas, G. Catania, A. Decelle, and B. Seoane, Explaining the effects of non-convergent sampling in the training of energy-based models, arXiv preprint arXiv:2301.09428 (2023).
- [28] J. Sohl-Dickstein, E. Weiss, N. Maheswaranathan, and S. Ganguli, Deep unsupervised learning using nonequilibrium thermodynamics, in *International Conference on Machine Learning* (PMLR, 2015) pp. 2256–2265.
- [29] B. Bravi, J. Tubiana, S. Cocco, R. Monasson, T. Mora, and A. M. Walczak, Rbm-mhc: a semi-supervised machine-learning method for sample-specific prediction of antigen presentation by hla-i alleles, Cell systems **12**, 195 (2021).
- [30] J. Fernandez-de Cossio-Diaz, P. Hardouin, F.-X. Lyonnet du Moutier, A. Di Gioacchino, B. Marchand, Y. Ponty, B. Sargueil, R. Monasson, and S. Cocco, Designing molecular rna switches with restricted boltzmann machines, bioRxiv , 2023 (2023).
- [31] H. Larochelle, M. Mandel, R. Pascanu, and Y. Bengio, Learning algorithms for the classification restricted boltzmann machine, The Journal of Machine Learning Research **13**, 643 (2012).
- [32] J. Fernandez-de Cossio-Diaz, S. Cocco, and R. Monasson, Disentangling representations in restricted boltzmann machines without adversaries, Physical Review X **13**, 021003 (2023).
- [33] L. Dabelow and M. Ueda, Three learning stages and accuracy–efficiency tradeoff of restricted boltzmann machines, Nature communications **13**, 5474 (2022).
- [34] A. P. Muntoni, A. Pagnani, M. Weigt, and F. Zamponi, adabmdca: adaptive boltzmann machine learning for biological sequences, BMC bioinformatics **22**, 1 (2021).
- [35] Y. LeCun, L. Bottou, Y. Bengio, and P. Haffner, Gradient-based learning applied to document recognition, Proceedings of the IEEE **86**, 2278 (1998).
- [36] . G. P. Consortium *et al.*, A global reference for human genetic variation, Nature **526**, 68 (2015).
- [37] E. Drula, M.-L. Garron, S. Dogan, V. Lombard, B. Henrissat, and N. Terrapon, The carbohydrate-active enzyme database: functions and literature, Nucleic acids research **50**, D571 (2022).
- [38] A. Yale, S. Dash, R. Dutta, I. Guyon, A. Pavao, and K. P. Bennett, Generation and evaluation of privacy preserving synthetic health data, Neurocomputing **416**, 244 (2020).
- [39] N. Béreux, A. Decelle, C. Furtlehner, and B. Seoane, Learning a restricted Boltzmann machine using biased Monte Carlo sampling, SciPost Phys. **14**, 032 (2023).
- [40] Z. Lin, H. Akin, R. Rao, B. Hie, Z. Zhu, W. Lu, N. Smetanin, R. Verkuil, O. Kabeli, Y. Shmueli, *et al.*, Evolutionary-scale prediction of atomic-level protein structure with a language model, Science **379**, 1123 (2023).
- [41] B. L. Cantarel, P. M. Coutinho, C. Rancurel, T. Bernard, V. Lombard, and B. Henrissat, The carbohydrate-active enzymes database (cazy): an expert resource for glycogenomics, Nucleic acids research **37**, D233 (2009).
- [42] R. C. Edgar, Muscle: a multiple sequence alignment method with reduced time and space complexity, BMC bioinformatics **5**, 1 (2004).

- [43] A. Baronchelli, E. Caglioti, and V. Loreto, Measuring complexity with zippers, *European journal of physics* **26**, S69 (2005).
- [44] R. Liao, S. Kornblith, M. Ren, D. J. Fleet, and G. Hinton, Gaussian-bernoulli rbms without tears, arXiv preprint arXiv:2210.10318 (2022).
- [45] J. Xie, Y. Zhu, J. Li, and P. Li, A tale of two flows: cooperative learning of langevin flow and normalizing flow toward energy-based model, arXiv preprint arXiv:2205.06924 (2022).
- [46] T. Bonnaire, A. Decelle, and N. Aghanim, Cascade of phase transitions for multiscale clustering, *Phys. Rev. E* **103**, 012105 (2021).
- [47] K. Rose, E. Gurewitz, and G. C. Fox, Statistical mechanics and phase transitions in clustering, *Phys. Rev. Lett.* **65**, 945 (1990).
- [48] N. Le Roux and Y. Bengio, Representational power of restricted boltzmann machines and deep belief networks, *Neural computation* **20**, 1631 (2008).
- [49] D. J. Thouless, P. W. Anderson, and R. G. Palmer, Solution of 'solvable model of a spin glass', *Philosophical Magazine* **35**, 593 (1977).
- [50] T. Tanaka, Information geometry of mean-field approximation, *Neural Computation* **12**, 1951 (2000).
- [51] M. Yasuda, Y. Kabashima, and K. Tanaka, Replica plefka expansion of ising systems, *Journal of Statistical Mechanics: Theory and Experiment* **2012**, P04002 (2012).
- [52] T. Tanaka, Mean-field theory of boltzmann machine learning, *Physical Review E* **58**, 2302 (1998).
- [53] F. Morcos, A. Pagnani, B. Lunt, A. Bertolino, D. S. Marks, C. Sander, R. Zecchina, J. N. Onuchic, T. Hwa, and M. Weigt, Direct-coupling analysis of residue coevolution captures native contacts across many protein families, *Proceedings of the National Academy of Sciences* **108**, E1293 (2011).
- [54] J. Tubiana, *Restricted Boltzmann machines : from compositional representations to protein sequence analysis*, Theses, Université Paris sciences et lettres (2018).
- [55] E. W. Tramel, M. Gabrié, A. Manoel, F. Caltagirone, and F. Krzakala, Deterministic and generalized framework for unsupervised learning with restricted Boltzmann machines, *Physical Review X* **8**, 041006 (2018).
- [56] A. Maillard, L. Foini, A. L. Castellanos, F. Krzakala, M. Mézard, and L. Zdeborová, High-temperature expansions and message passing algorithms, *Journal of Statistical Mechanics: Theory and Experiment* **2019**, 113301 (2019).
- [57] M. Gabrié, E. W. Tramel, and F. Krzakala, Training restricted Boltzmann machine via the Thouless-Anderson-Palmer free energy, in *Advances in neural information processing systems* (2015) pp. 640–648.
- [58] A. Decelle, G. Fissore, and C. Furtlehner, Thermodynamics of restricted boltzmann machines and related learning dynamics, *Journal of Statistical Physics* **172**, 1576 (2018).
- [59] J. Tubiana and R. Monasson, Emergence of compositional representations in restricted boltzmann machines, *Physical review letters* **118**, 138301 (2017).
- [60] T. Yokota, Ordered phase for the infinite-range potts-glass model, *Phys. Rev. B* **51**, 962 (1995).
- [61] T. Plefka, Convergence condition of the tap equation for the infinite-ranged ising spin glass model, *Journal of Physics A: Mathematical and General* **15**, 1971 (1982).
- [62] A. Georges and J. S. Yedidia, How to expand around mean-field theory using high-temperature expansions, *Journal of Physics A: Mathematical and General* **24**, 2173 (1991).
- [63] F. Zamponi, Mean field theory of spin glasses, arXiv preprint arXiv:1008.4844 (2010).
- [64] R. Vicedomini, J. Bouly, E. Laine, A. Falciatore, and A. Carbone, Multiple Profile Models Extract Features from Protein Sequence Data and Resolve Functional Diversity of Very Different Protein Families, *Molecular Biology and Evolution* **39**, 10.1093/molbev/msac070 (2022).
- [65] M. Ester, H.-P. Kriegel, J. Sander, and X. Xu, A density-based algorithm for discovering clusters in large spatial databases with noise, in *Proceedings of the Second International Conference on Knowledge Discovery and Data Mining*, KDD'96 (AAAI Press, 1996) p. 226–231.
- [66] A. Sancar, Structure and function of dna photolyase and cryptochrome blue-light photoreceptors, *Chemical Reviews* **103**, 2203 (2003), pMID: 12797829, <https://doi.org/10.1021/cr0204348>.
- [67] K. Brettel and M. Byrdin, Reaction mechanisms of dna photolyase, *Current opinion in structural biology* **20**, 693–701 (2010).
- [68] I. Chaves, R. Pokorný, M. Byrdin, N. Hoang, T. Ritz, K. Brettel, L.-O. Essen, G. T. J. van der Horst, A. Batschauer, and M. Ahmad, The cryptochromes: Blue light photoreceptors in plants and animals, *Annual Review of Plant Biology* **62**, 335 (2011), pMID: 21526969, <https://doi.org/10.1146/annurev-arplant-042110-103759>.
- [69] M. Jaubert, J.-P. Bouly, M. R. d'Alcalà, and A. Falciatore, Light sensing and responses in marine microalgae, *Current Opinion in Plant Biology* **37**, 70 (2017).
- [70] H. Huang, *Statistical mechanics of neural networks* (Springer, 2021).
- [71] W. P. Russ, M. Figliuzzi, C. Stocker, P. Barrat-Charlaix, M. Socolich, P. Kast, D. Hilvert, R. Monasson, S. Cocco, M. Weigt, *et al.*, An evolution-based model for designing chorismate mutase enzymes, *Science* **369**, 440 (2020).
- [72] Z. Wu, K. K. Yang, M. J. Liszka, A. Lee, A. Batzilla, D. Wernick, D. P. Weiner, and F. H. Arnold, Signal peptides generated by attention-based neural networks, *ACS Synthetic Biology* **9**, 2154 (2020).
- [73] N. Ferruz, S. Schmidt, and B. Höcker, Protgpt2 is a deep unsupervised language model for protein design, *Nature communications* **13**, 4348 (2022).
- [74] B. Huang, Y. Xu, X. Hu, Y. Liu, S. Liao, J. Zhang, C. Huang, J. Hong, Q. Chen, and H. Liu, A backbone-centred energy function of neural networks for protein design, *Nature* **602**, 523 (2022).
- [75] A. Madani, B. Krause, E. R. Greene, S. Subramanian, B. P. Mohr, J. M. Holton, J. L. Olmos Jr, C. Xiong, Z. Z. Sun, R. Socher, *et al.*, Large language models generate functional protein sequences across diverse families, *Nature Biotechnology* , 1 (2023).
- [76] E. Nijkamp, J. Ruffolo, E. N. Weinstein, N. Naik, and A. Madani, Progen2: exploring the boundaries of protein language models, arXiv preprint arXiv:2206.13517 (2022).
- [77] N. Koga, R. Tatsumi-Koga, G. Liu, R. Xiao, T. B. Acton, G. T. Montelione, and D. Baker, Principles for designing ideal protein structures, *Nature* **491**, 222 (2012).
- [78] Y.-R. Lin, N. Koga, R. Tatsumi-Koga, G. Liu, A. F. Clouser, G. T. Montelione, and D. Baker, Control over overall shape and size in de novo designed proteins, *Proceedings of the National Academy of Sciences* **112**, E5478 (2015).

- [79] P.-S. Huang, S. E. Boyken, and D. Baker, The coming of age of de novo protein design, *Nature* **537**, 320 (2016).
- [80] P.-S. Huang, K. Feldmeier, F. Parmeggiani, D. A. Fernandez Velasco, B. Höcker, and D. Baker, De novo design of a four-fold symmetric tim-barrel protein with atomic-level accuracy, *Nature chemical biology* **12**, 29 (2016).
- [81] S. E. Boyken, Z. Chen, B. Groves, R. A. Langan, G. Oberdorfer, A. Ford, J. M. Gilmore, C. Xu, F. DiMaio, J. H. Pereira, *et al.*, De novo design of protein homo-oligomers with modular hydrogen-bond network-mediated specificity, *Science* **352**, 680 (2016).

ACKNOWLEDGMENTS

We acknowledge financial support by the Comunidad de Madrid and the Complutense University of Madrid (UCM) through the Atracción de Talento programs (Refs. 2019-T1/TIC-13298 and 2019-T1/TIC-12776), the Banco Santander and the UCM (grant PR44/21-29937), and Ministerio de Economía y Competitividad, Agencia Estatal de Investigación and Fondo Europeo de Desarrollo Regional (Ref. PID2021-125506NA-I00).

CODE AVAILABILITY

The python code for the present work can be found at the link <https://github.com/rossetl/FeF.git>.

Appendix A: Dataset description

1. MNIST dataset

The MNIST dataset [35] consists of 28×28 grayscale images of handwritten digits tagged with a label indicating the digit represented, from 0 to 9. We first extracted a training set and a test set of respectively 10000 and 2000 images, and we then binarized the data by setting each pixel to 1 if the normalized value was above 0.3, and to 0 otherwise. To be fed to the RBM, the images have to be flattened into 784-dimensional binary vectors.

2. Human Genome Dataset (HGD)

The Human Genome dataset (HGD) [36] represents the human genetic variations of a population of 5008 individuals sampled from 26 populations in Africa, East Asia, South Asia, Europe, and the Americas. Each sample is a sequence of 805 binary variables, $v_i \in \{0, 1\}$, representing the change alteration or not of a gene relative to a reference genetic sequence. Sequences are classified based on the continental origin of individuals. We trained the RBM on 4507 samples and retained 501 samples for the test set.

3. GH30 family

The glycoside hydrolases (EC 3.2.1.-), GH for short, are a family of enzymes that hydrolyze the glycosidic bond between two or more carbohydrates or between a carbohydrate and a non-carbohydrate moiety. GH30 is one of the GH families that has been divided into subfamilies in CAZy. It includes nine different subfamilies (GH30-1,..., GH30-9) corresponding to 11 different enzymatic chemical reactions. We created a training and test set of respectively 3922 and 975 annotated sequences from CAZy [37, 41], having care of reproducing the same samples-per-label proportion between training and test sets. The sequences were previously aligned in an MSA matrix using the MUSCLE algorithm [42] with default parameters. We then cleaned all MSA columns in which the proportion of gaps was above 70% of the entries. The resulting sequences have a length of $N_v = 430$, where each residue can take one over 21 possible values (20 amino acids + the alignment gap).

4. SAM domain

The SAM (S-Adenosyl methionine) riboswitch (RF00162) is found upstream of a number of genes which code for proteins involved in methionine or cysteine biosynthesis in Gram-positive bacteria. We downloaded the dataset from Rfam alongside the taxonomic classification of each sequence. Among all the sequences, we retained only those belonging to the five largest groups containing more than 100 sequences: Actinomycetota, Bacillota, Bacteroidota, Chloroflexi and Pseudomonadota. We then split the dataset into training and test set of respectively 4733 and 524 samples having the same proportion of data points across the categories. The aligned sequences have a length of $N_v = 108$, and each site can assume one of 5 possible states (the 4 nucleobases + the alignment gap).

The details about the composition of the training/testing sets used for each dataset can be found in Table I.

Appendix B: RBM training details

The hyperparameters used for the training processes discussed in this paper are given in Table II.

Appendix C: Tables

Appendix D: Quality scores

To assess the generation capabilities of the RBM, one can compute a set of observables on the generated dataset and the actual data and compare them [22]. In the plots of Figs. 3 and 4 we have considered the following scores:

TABLE I. Number of data samples for each category in the train and test sets for the used datasets.

MNIST										
Label	0	1	2	3	4	5	6	7	8	9
Train set count	1022	1078	1046	1031	965	916	972	1042	977	951
Test set count	188	224	218	191	220	174	208	178	197	202

HGD					
Label	African	American	East Asian	European	South Asian
Train set count	1184	622	912	910	879
Test set count	138	72	96	96	99

GH30									
Label	GH30_1	GH30_2	GH30_3	GH30_4	GH30_5	GH30_6	GH30_7	GH30_8	GH30_9
Train set count	886	287	1044	270	435	39	89	810	62
Test set count	221	71	260	67	108	9	22	202	15

SAM					
Label	Actinomycetota	Bacillota	Bacteroidota	Chloroflexi	Pseudomonadota
Train set count	549	3159	747	120	158
Test set count	61	351	82	13	17

TABLE II. Hyper-parameters of the RBMs used in this work.

dataset	epochs	minibatch size	total gradient updates	k	learning rate	N_h
MNIST (PCD)	30000	500	$6 \cdot 10^5$	100	10^{-2}	1024
HGD (PCD)	30000	4507	$3 \cdot 10^4$	100	10^{-2}	1024
GH30 (PCD)	30000	1961	$6 \cdot 10^4$	100	10^{-2}	1024
SAM (PCD)	30000	1000	$1.2 \cdot 10^5$	100	10^{-2}	100 / 1000
MNIST (F&F)	30000	500	$6 \cdot 10^5$	10	10^{-2}	1024
HGD (F&F)	30000	4507	$3 \cdot 10^4$	10	10^{-2}	1024
GH30 (F&F)	30000	1961	$6 \cdot 10^4$	10	10^{-2}	1024
SAM (F&F)	30000	1000	$1.2 \cdot 10^5$	10	10^{-2}	100 / 1000

- **Error on the spectrum (ϵ^S):** Given a data matrix $X \in \mathbb{R}^{M \times N_v}$, its singular value decomposition (SVD) consists in writing X as the matrix product

$$X = USV^T,$$

where $U \in \mathbb{R}^{M \times M}$, S is an $M \times N_v$ matrix with the singular values of X in the diagonal, and $V \in \mathbb{R}^{N_v \times N_v}$. Let us call $N_s = \min(M, N_v)$. Once we sort the singular values $\{s_i\}$ such that $s_1 > s_2 > \dots > s_{N_s}$, we can define the error of the spectrum as

$$\epsilon^S = \frac{1}{N_s} \sum_{i=1}^{N_s} (s_i^{\text{data}} - s_i^{\text{gen}})^2, \quad (\text{D1})$$

where $\{s_i^{\text{data}}\}$ are the singular values of the true data

and $\{s_i^{\text{gen}}\}$ are the singular values of the generated dataset.

- **Error on the entropy (ΔS):** We approximate the entropy of a given dataset by its byte size when compressed with gzip [43]. In particular, if S^{data} is the estimated entropy of the true data and S^{gen} is the estimated entropy of the generated data, we define the error of entropy as

$$\Delta S = \left(\frac{S^{\text{gen}}}{S^{\text{data}}} - 1 \right)^2. \quad (\text{D2})$$

A large ΔS indicates that the generated set lacks diversity or that the generated samples are less “ordered” than the dataset.

- **Error on the Adversarial Accuracy Indicator (ϵ^{AAI}):** This score was introduced in Ref. [38] to quantify the similarity and “privacy” of data drawn from a generative model with respect to the training set. We first construct a dataset obtained by joining the real dataset with the generated dataset, and then compute the matrix of distances between each pair of data points. We denote by P_{GG} the probability that a generated datapoint has as the nearest neighbour a generated data and by P_{DD} the probability that a true datapoint has as the near-

est neighbour a true data. In the best case, when the generated data are statistically indistinguishable from the true ones, we have $P_{\text{GG}} = P_{\text{DD}} = 0.5$. Therefore, we can define the error of the Adversarial Accuracy Indicator as follows:

$$\epsilon^{\text{AAI}} = \frac{1}{2} [(P_{\text{GG}} - 0.5)^2 + (P_{\text{DD}} - 0.5)^2]. \quad (\text{D3})$$

Appendix E: Supplementary figures

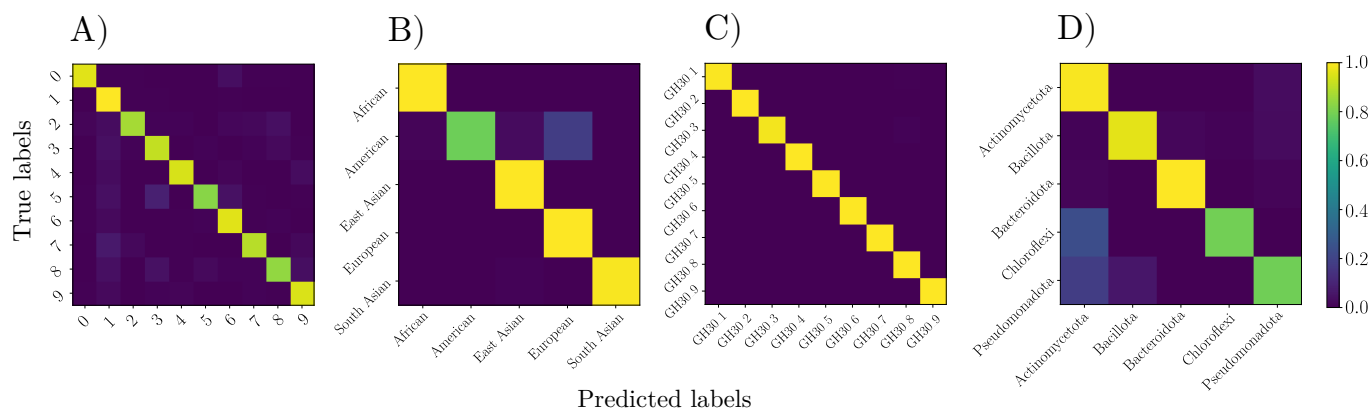


FIG. 7. Confusion matrices for the label classification using F&F on the test sets of A) MNIST, B) HGD, C) GH30 and D) SAM.

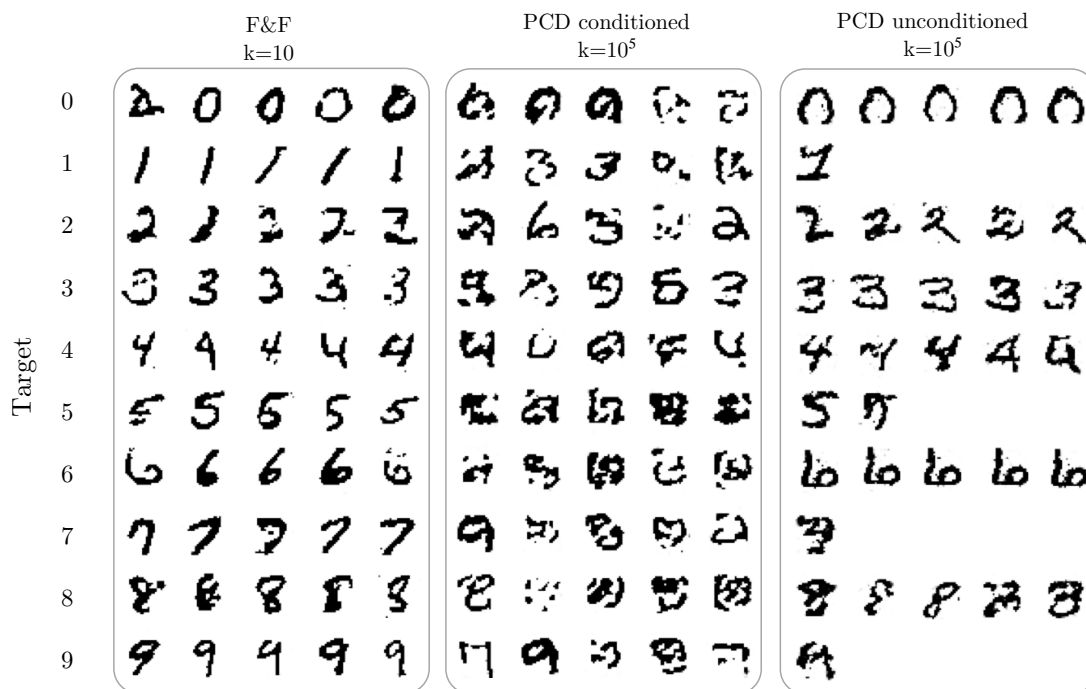


FIG. 8. MNIST images created using different methods for specific labels. From left to right, the first box shows the output of F&F for $k = 10$ MCMC steps. The images in the second box are generated using a PCD-RBM after 10^5 MCMC steps when the Markov chains are clamped to a specific label value. The third box shows the result of sampling with a PCD-RBM, where we also sample the labels when running the Markov chains. An empty slot means that the RBM never provided the appropriate sample in our tests after 10^5 MCMC steps.

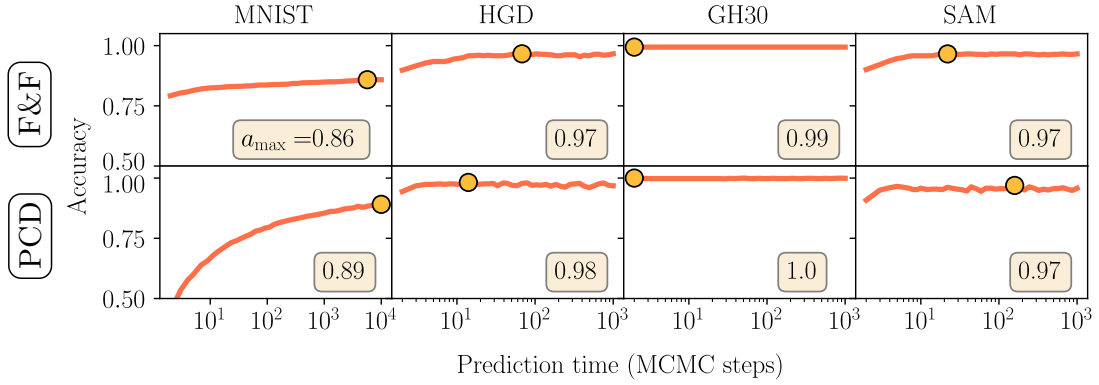


FIG. 9. Test accuracies obtained by the most trained models in the task of label prediction as a function of the prediction time for all the considered datasets. The yellow boxes in the bottom-right corner of the insets indicate the maximum accuracy achieved (a_{\max}), corresponding to the big yellow dots.

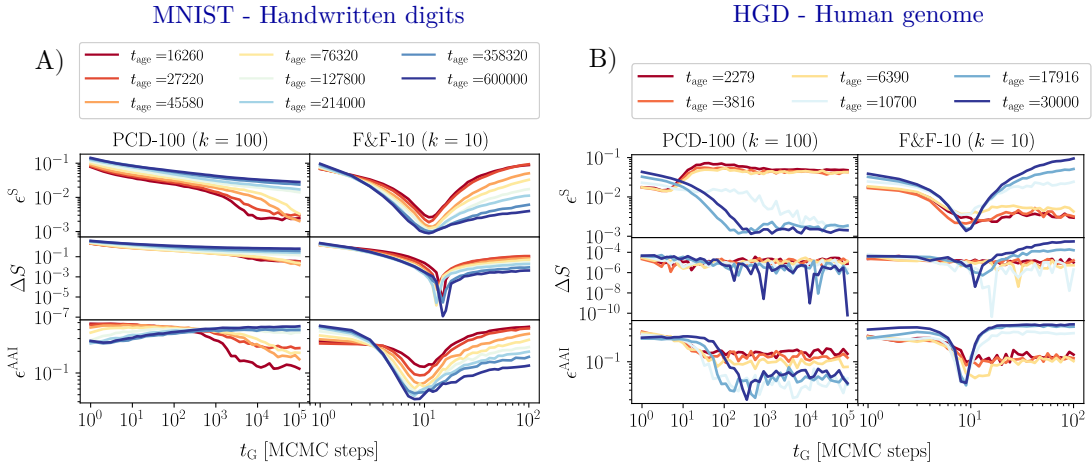


FIG. 10. Comparison of the scores on the generated data between PCD-100 and F&F-10 RBMs as a function of the generation time (t_G) for A) MNIST and B) HGD. All the scores are computed by comparing the test set with an identical (in terms of samples for each category) generated dataset. The samples of each category of the dataset have been compared with the corresponding samples of the synthetic data, and the curves shown in the figure represent the average scores across the different categories. The different colours of the curves represent different training times (t_{age}), expressed in terms of gradient updates. Notice that for the PCD-RBM the generation time ranges up to 10^5 MCMC updates, while for the F&F-RBM it only reaches 10^2 MCMC updates. The generated samples shown in Figs. 1-A and 3 correspond to the darkest blue curves in correspondence of the indicated generation time t_G .

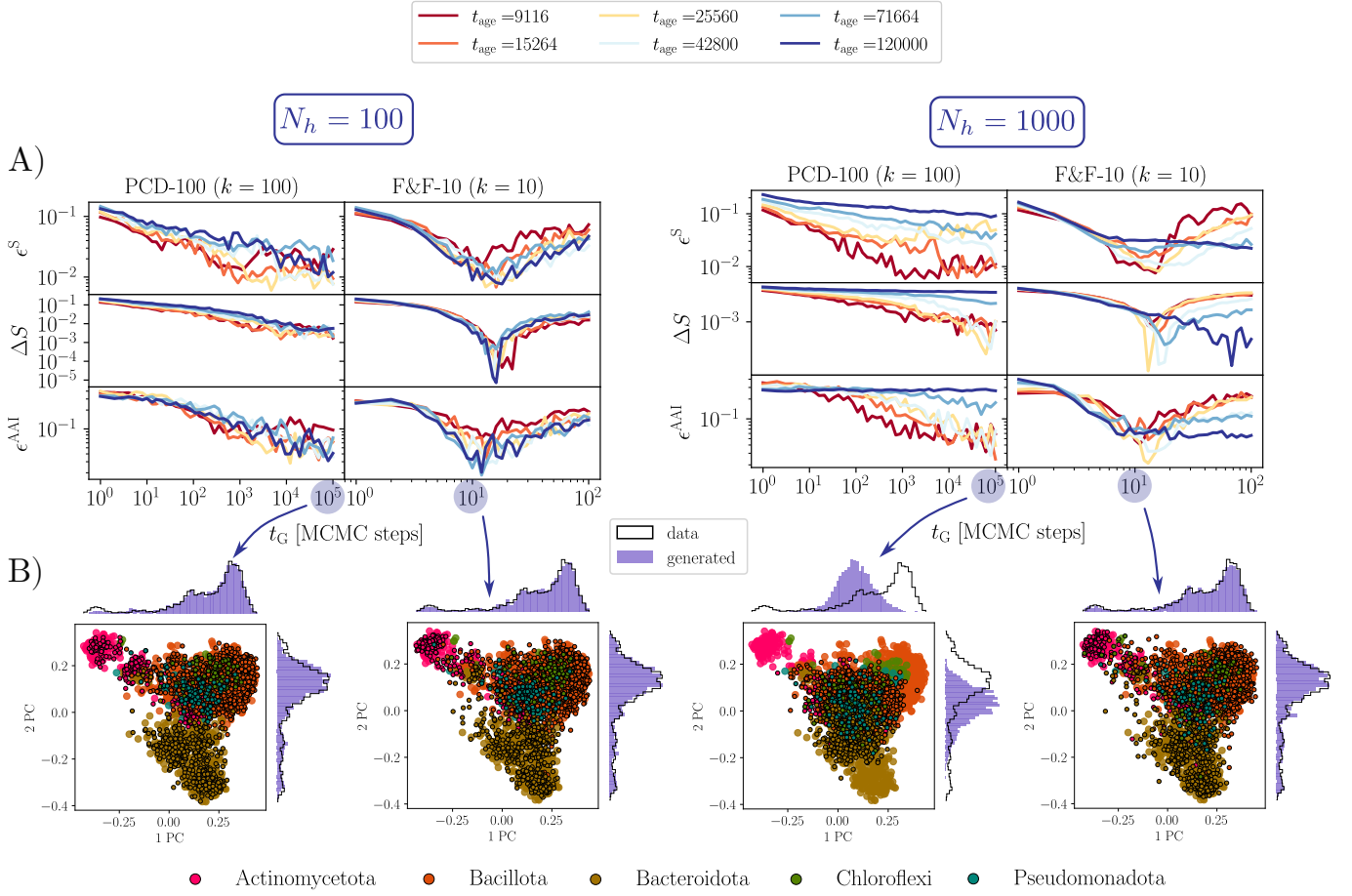


FIG. 11. Example of instability of the PCD RBM on the SAM dataset when the number of hidden nodes, N_h , is changed. In A) we show the comparison between the score curves of PCD and F&F RBMs for $N_h = 100$ (left) and $N_h = 1000$ (right). In B), instead, we show the data generated with the most trained model (dark-blue curve) after 10^5 and 10 MCMC updates for PCD and F&F, respectively. The data are projected along the two principal components of the dataset's PCA. The big colored dots represent the true data, whereas the contoured dots represent the generated samples. Different colors correspond to different categories. The histograms on the sides show the distributions of the true data (black profile) and the synthetic data (violet-shaded area) projected along the two principal directions of the dataset. For $N_h = 100$ we obtained a properly trained model using both the training methods, and these models are those shown in the main text. Conversely, when we set $N_h = 1000$ we obtained a PCD RBM model displaying huge thermalization times after just a few training epochs, while F&F still managed to yield a model whose generated data correctly span the whole data space.